Processing and Application of Ceramics 19 [4] (2025) 367–373
https://doi.org/10.2298/PAC2504367M

Structural and dual mode up-conversion and down-shifting properties of Er^{3+}/Yb^{3+} activated $SrTiO_3$ phosphor

Biswaranjan Mishra[1], Deva Sucharitha Chakram[1], Bheeshma Pratap Singh[1,*], Kavitha Chandu[1], Kagola Upendra Kumar[2], Madhavaprasad Dasari[1,*]

[1]*Department of Physics, GITAM School of Science, GITAM (Deemed to be University) Visakhapatnam-530045, India*
[2]*Department of Physics, School of Applied Sciences, REVA University, Bangalore - 560 064, India*

Received 23 September 2025; Received in revised form 21 November 2025; Accepted 5 December 2025

Abstract

Dual-mode down-shifting and up-converting $SrTiO_3:Er^{3+}/Yb^{3+}$ doped phosphor was synthesized via the solid-state ceramic route. Structural characterization via XRD confirms formation of the cubic $SrTiO_3$ perovskite phase (space group $Pm\bar{3}m$) with small amount of secondary $Yb_2Ti_2O_7$ phase. SEM study confirms the irregular semispherical micrograins. UV-Vis data confirms the absorption of Yb^{3+} at 980 nm. Up-conversion study under the 980 nm laser irradiation exhibits the strong green colour bands at 526 and 548 nm as well as a red emission band at 660 nm, which arises due to the electronic transitions corresponding to $^2H_{11/2} \rightarrow {}^4I_{15/2}$, $^4S_{3/2} \rightarrow {}^4I_{15/2}$ and $^4F_{9/2} \rightarrow {}^4I_{15/2}$. The observed green and red colour bands were predominantly ascribed to the phenomenon of two-photon absorption. Also, down-shifting under 980 nm excitation exhibits a strong emission band at 1535 nm, which is the characteristic transition of the Er^{3+} ion arising from $^4I_{13/2} \rightarrow {}^4I_{15/2}$. Lifetime analysis was executed to study the decay dynamics of the green colour emission bands at ~545 nm ($^4S_{3/2} \rightarrow {}^4I_{15/2}$). Colour tuning was observed in the CIE coordinates at different laser input powers. Synthesized phosphor materials may be utilized as the green colour phosphor and in optical communications.

Keywords: *Er^{3+}/Yb^{3+} $SrTiO_3$, energy transfer, dual mode emission, CIE coordinate*

I. Introduction

Rare earth activated up-converting nanomaterials have shown possible promising applications in solar cells, temperature sensing, display and bioimaging due to their intriguing features of converting near infrared light into ultraviolet and visible light via multi-photon energy transfer processes [1–10]. The inorganic matrices, which accommodate activator ions, are usually termed as host matrices. There are various inorganic host matrices, such as Y_2O_3, Gd_2O_3, ZrO_2, YVO_4, $CaMoO_4$, YPO_4 and $LaPO_4$, reported for the up-conversion properties due to their low phonon energies [11–16]. Low phonon energy of the host material improves the radiative transition probabilities. Up-converting nanoparticles exhibit anti-Stokes emission under 980 nm excitation covering the bioimaging window.

Strontium titanate ($SrTiO_3$) is a promising host matrix for up-conversion applications due to its high thermal, chemical and physical stability, optical transparency in the visible region, and low phonon energy [17]. Trivalent erbium ions have been extensively used for the up-conversion emission under the 980 nm excitation. The metastable energy levels $^4I_{11/2}$ and $^4I_{9/2}$ of erbium ions can be populated under 980 nm. Trivalent Yb^{3+} ion acts as a sensitizer which transfers its energy to Er^{3+} ion since Yb^{3+} has a high absorption cross section at 980 nm, which leads to the enhanced visible luminescence [18].

Synthesis route and the nanophosphor materials with controlled shape and size have been crucial due to the correlation between photoluminescence and crystal structure. Several synthesis protocols, namely hydro and solvothermal, sol-gel and combustion, have been reported for $SrTiO_3$ nanoparticles [19]. These routes fetch

* Corresponding author: +91 9348811777
e-mail: *madhavaprasaddasari@gmail.com* (M. Dasari)
bsingh@gitam.edu (B.P. Singh)

the controlled shape and size, high homogeneity and less agglomeration of the nanoparticles. However, several defects are also associated with these routes, which hamper the luminescence intensity significantly.

In this work, Er^{3+} and Yb^{3+} co-doped $SrTiO_3$ phosphors were successfully synthesized via a conventional solid-state ceramic route. The study provides a comprehensive investigation of the structural, morphological and bimodal optical properties encompassing both up-conversion (UC) and down-conversion (DC) emissions of the prepared phosphor system. Incorporation of Er^{3+} and Yb^{3+} ions into the $SrTiO_3$ host matrix is of particular importance due to their well-known role in facilitating efficient energy transfer processes, which significantly enhance luminescence performance.

II. Experimental

2.1. Synthesis

$SrTiO_3$ doped with 2 at.% Er^{3+} and 20 at.% Yb^{3+} ($SrTiO_3$: $0.02Er^{3+}/0.20Yb^{3+}$ phosphor) was synthesized using a conventional solid-state ceramic route. For a typical 4 g batch, stoichiometric amounts of $SrCO_3$ (1.636 g), TiO_2 (1.1348 g), Er_2O_3 (0.1088 g) and Yb_2O_3 (1.1196 g) were thoroughly mixed in an agate mortar with acetone as the grinding medium for approximately 3 h to ensure homogeneity. The resulting mixture was pre-calcined at 700 °C for 4 h in a temperature-controlled furnace. After natural cooling to room temperature, the calcined powders were uniaxially pressed at 4 MPa to form pellets with diameter of 10 mm using a 4% PVA solution as a temporary binder. The pellets were subsequently heated at 600 °C for 1 h to remove the binder and then sintered at 1200 °C for 6 h to promote complete phase formation.

2.2. Characterization techniques

X-ray diffraction (XRD) pattern was recorded on a Bruker D8 Advance power diffractometer at room temperature. Fourier transform infrared (FTIR) study has been carried out by ATR-FTIR Spectrometer, ALPHA-II. Field emission scanning electron microscopy (FE-SEM, Zeiss Ultra 55) equipped with energy dispersive X-ray (EDX) was used to observe the morphology of the samples. UV-Visible spectrum and absorption studies were performed with Shimadzu UV-2600i. The up-conversion (UC) spectra were collected using an EDINBURGH instruments FLS1000 spectrometer, equipped with a 980 nm continuous-wave (CW) laser diode and a Hamamatsu R955 photomultiplier tube (PMT). The 980 nm laser beam was focused onto the sample, which produces a spot size with a diameter of approximately 1 mm. Decay time of green emitting level was recorded with an Edinburgh instrument FL1000 under the 980 nm excitation in pulse mode. Down-shifting emission spectrum was recorded with a 450 W Xenon flash lamp.

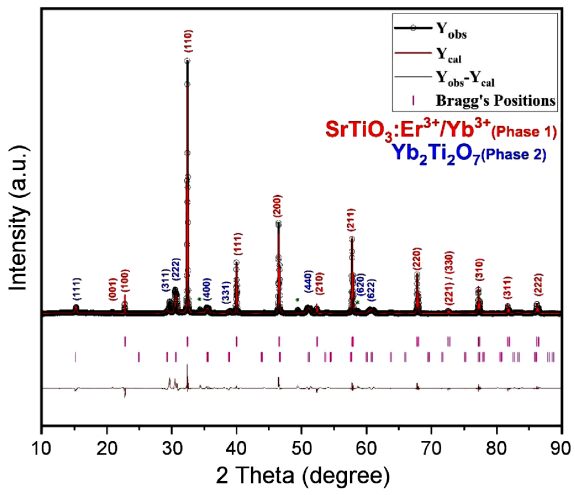

Figure 1. XRD pattern of the studied sample and Rietveld refinement

III. Results and discussion

3.1. Structural characterization

XRD pattern of the $SrTiO_3$:$0.02Er^{3+}/0.20Yb^{3+}$ is shown in Fig. 1 and confirms the presence of two phases, namely dominant cubic $SrTiO_3$ perovskite and secondary $Yb_2Ti_2O_7$ pyrochlore structure.

The Rietveld refinement was used to determine lattice parameters and content of cubic $SrTiO_3$ and pyrochlore $Yb_2Ti_2O_7$ phases. Six coefficient polynomials were used to model the peaks profile using pseudo-Voigt function. Most of the XRD peaks of the $SrTiO_3$:$0.02Er^{3+}/0.20Yb^{3+}$ sample match the main diffraction peaks of the $SrTiO_3$ cubic structure, which is perovskite with the space group of $Pm\bar{3}m$. Moreover, the secondary pyrochlore $Yb_2Ti_2O_7$ phase with Fdm was also detected with the Rietveld analysis and indexing for both $SrTiO_3$ and $Yb_2Ti_2O_7$ phases was executed [20]. The Rietveld refinement data reveals the presence of 79.98 wt.% of $SrTiO_3$ and 21.02 wt.% of $Yb_2Ti_2O_7$ (Table 1). The existence of a small amount of the secondary phase may arise due to the lower sintering temperature (1200 °C in our case). The small amount of the secondary phase does not alter optical properties and further confirms the successful incorporation of Er^{3+} and Yb^{3+} ions in the $SrTiO_3$ crystal lattice. Tritt *et al.* [21] showed that the crystallization of single phase perovskite structure can be obtained by sintering at 1400 °C. The ionic radii of Sr^{2+} in twelve-fold coordination and Ti^{4+} in six-fold coordination are 1.44 and 0.605 Å, respectively. Rare earth ions Er^{3+} (0.89 Å) and Yb^{3+} (0.868 Å) can be incorporated on both A- and B-sites of the perovskite cell. However, they most likely substitute Sr^{2+} at A-site of the cubic $SrTiO_3$ crystal structure, since it provides the best compatibility for their accommodation in the crystal lattice because of the similar ionic radii [22].

FTIR spectrum of the $SrTiO_3$:Er^{3+}/Yb^{3+} sample was shown in Fig. 2. The spectrum reveals the presence of a strong band at ~527 cm^{-1}, ascribed to the stretching

Table 1. Rietveld refined lattice parameters and content of the $SrTiO_3:Er^{3+}/Yb^{3+}$ and $Yb_2Ti_2O_7$ phases

Sample details	Lattice parameters [Å]	Cell volume [Å^3]	Phase content [wt.%]
$SrTiO_3:Er^{3+}/Yb^{3+}$ $Pm\bar{3}m$ (cubic)	a = 3.9048	59.54	78.98
$Yb_2Ti_2O_7$ $Fd\bar{3}m$ (pyrochlore)	a = 10.1124	1034.11	21.02

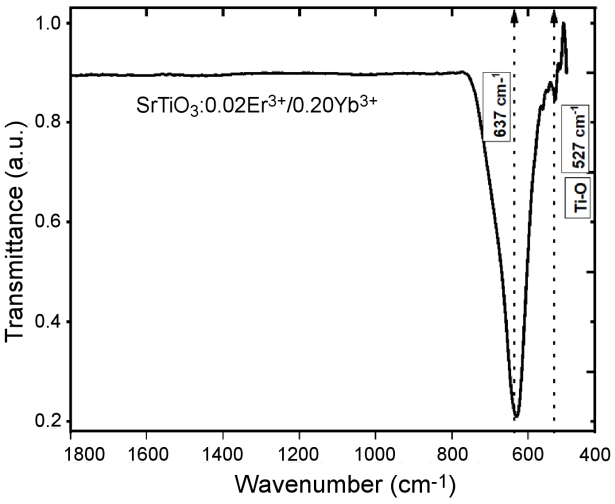

Figure 2. FTIR spectrum of the $SrTiO_3:0.02Er^{3+}/0.20Yb^{3+}$ phosphor

vibration of Ti–O bond. An intense and wide vibrational band appearing between ~800 and 500 cm^{-1} corresponds to the $SrTiO_3$ stretching vibrations, which further confirms the formation of $SrTiO_3$ [23]. Harooni and Attar [24] reported FTIR study for the Mg doped $SrTiO_3$ thin films and observed the absorption at 855 cm^{-1} which is due to the TiO_6 octahedron vibration. The absorption peak with feeble intensity at 798 cm^{-1} arises namely because of the Sr–Ti–O stretching vibrations. Similar observations were reported for the Ce doped $SrTiO_3$ perovskite oxide [25].

Surface morphology of the $SrTiO_3:Er^{3+}/Yb^{3+}$ ceramics sintered at 1200 °C for 6 h is presented in Fig. 3a. The SEM micrograph, captured using backscattered electron (BSE) imaging on fractured pellets, clearly highlights the microstructural features of the sintered ceramics. The grains predominantly exhibit irregular polyhedral shape, which is typical of high-temperature solid-state reactions and indicates significant grain growth and densification during sintering. The microstructure shows grains of varying dimensions, suggesting a non-uniform grain growth mechanism, often associated with dopant-induced lattice distortions or local inhomogeneities within the ceramic matrix.

The elemental composition of the prepared ceramics was further examined using energy-dispersive X-ray spectroscopy (EDX), as shown in Fig. 4. The spectrum confirms the presence of Sr, Ti and O corresponding to the $SrTiO_3$ host lattice, along with clear signatures of the incorporated rare-earth dopants Er and Yb. No extraneous or impurity peaks were observed, indicating the chemical purity and successful incorporation of the dopants. Elemental mapping of Sr, Ti, O, Er and Yb, shown in Fig. 4, reveals a homogeneous spatial distribution of all constituent elements throughout the ceramic microstructure. The uniform dispersion of Er^{3+} and Yb^{3+} within the $SrTiO_3$ lattice further supports their effective substitution at appropriate lattice sites, ensuring consistent optical and structural behaviour across

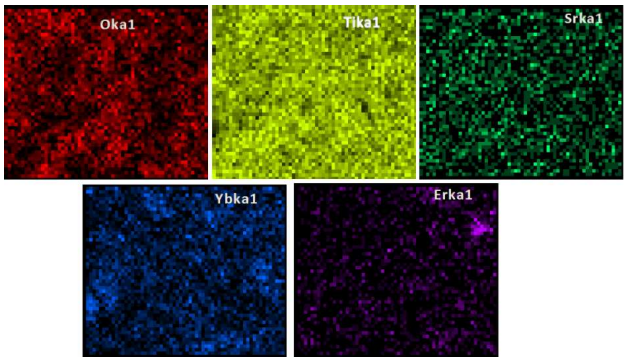

Figure 4. Elemental mapping of elements in the $SrTiO_3$, namely O, Ti, Sr, Yb and Er

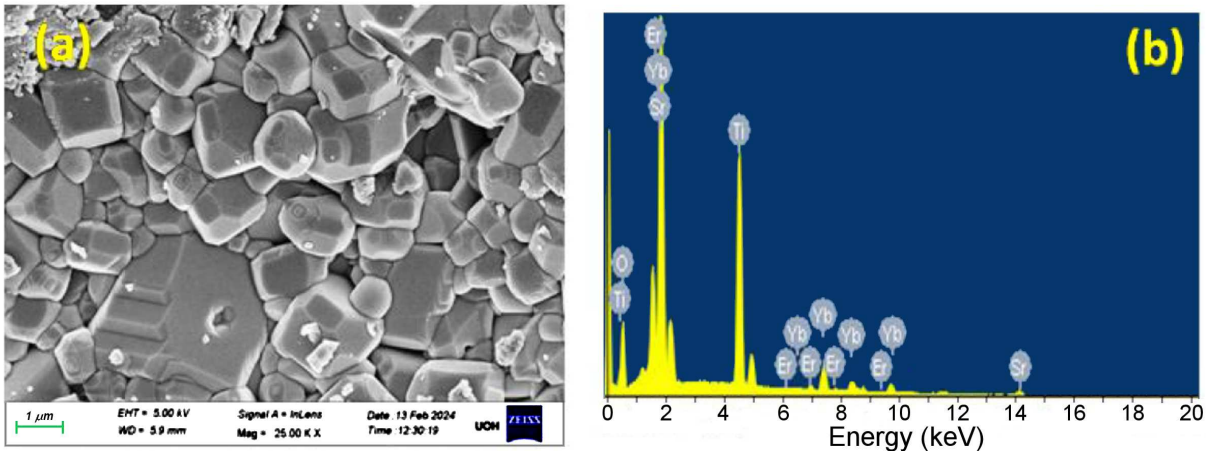

Figure 3. FESEM micrograph (a) and EDX spectra (b) of the $SrTiO_3:0.02Er^{3+}/0.20Yb^{3+}$ phosphor

the sample. This homogeneous distribution also indicates that the applied synthesis route leads to the efficient dopant incorporation without phase segregation or clustering.

3.2. Optical properties

Absorption spectrum of Er^{3+}/Yb^{3+} doped $SrTiO_3$, shown in Fig. 5, exhibits an absorption peak at 980 nm, which refers to the $^2F_{7/2} \rightarrow {}^2F_{5/2}$ electronic transition of the Yb^{3+} ion (Fig. 6). The peak at 526 nm corresponds to Er^{3+} ion absorption $^4I_{15/2} \rightarrow {}^2H_{11/2}$ (Fig. 6). The absorption peak centred at 980 nm for the sample co-doped with Er^{3+}/Yb^{3+} clearly validates that Yb^{3+} ion acts as a brilliant sensitizer for the absorption of the 980 nm laser light.

Up-conversion spectra were recorded under the 980 nm excitation wavelength at room temperature. There is a rise in up-conversion emission intensity with a rise in input laser power as the laser input power was varied from 50 to 500 mW with a step of 25 mW (Fig. 7). The sample fetches intensive green and red

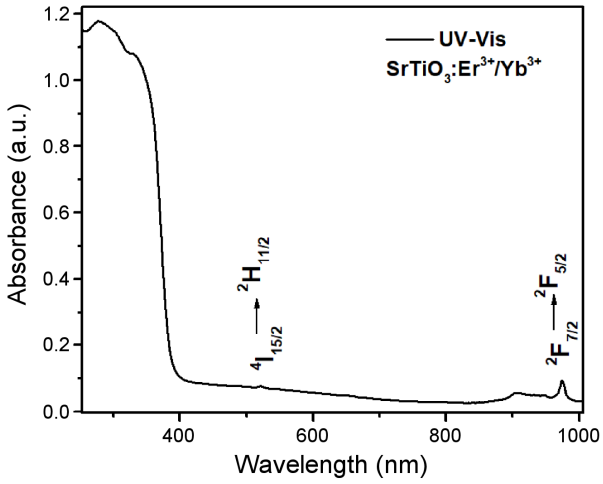

Figure 5. UV-Vis spectrum of the $SrTiO_3$:0.02Er^{3+}/0.20Yb^{3+} phosphor

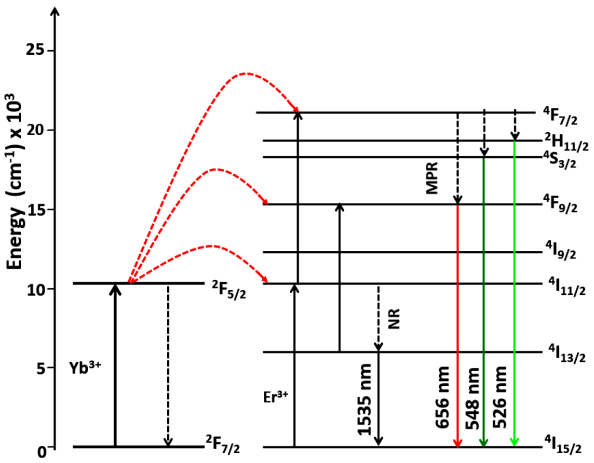

Figure 6. Energy transfer mechanisms in the $SrTiO_3$:0.02Er^{3+}/0.20Yb^{3+} phosphor

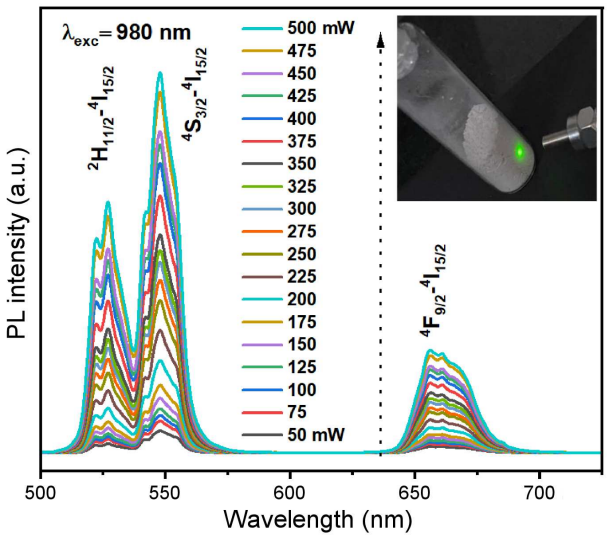

Figure 7. Power-dependent up-conversion spectra of $SrTiO_3$:0.02Er^{3+}/0.20Yb^{3+}

emissions even at very low power ~50 mW, which is very much vital for the device and biomedical applications [26]. The emission spectra exhibit the characteristic green and red colour bands appearing at 526, 548 and 660 nm (Fig. 7). These electronic bands of Er^{3+} ions arise due to transitions corresponding to $^2H_{11/2} \rightarrow {}^4I_{15/2}$, $^4S_{3/2} \rightarrow {}^4I_{15/2}$ and $^4F_{9/2} \rightarrow {}^4I_{15/2}$ (Fig. 6). The green energy bands at 526 and 548 nm are thermally coupled with each other and can be employed for the temperature sensing application. The powder sample shows a strong green emission at 548 nm under the 980 nm excitation.

In order to understand the up-conversion phenomena of perceived green bands and red bands, the up-conversion intensity varies with laser input power as $I_{up} \propto P_n$, where n refers to the number of pump photons absorbed, P refers to the laser input power and I_{up} is the up-conversion intensity.

Under the 980 nm CW laser excitation, Yb^{3+} ions get promoted from the ground state absorption (GSA) process, and Yb^{3+} and Er^{3+} ions are excited to their corresponding higher energy states, for Yb^{3+}, $^2F_{7/2} \rightarrow {}^2F_{5/2}$ and for Er^{3+}, $^4I_{15/2} \rightarrow {}^4I_{11/2}$ (Fig. 6). Excited state Yb^{3+} ions transfer their energy to the neighbouring Er^{3+} ion to populate the $^4F_{7/2}$ level, and Yb^{3+} ions return to the ground state $^2F_{7/2}$. Additional energy transfer from $^4I_{11/2}$ results in the increase of number of photons at the $^4F_{7/2}$ energy level. The multiphonon vibrational relaxation occurs and takes place from the green emission bands (526 and 548 nm), which arise from the electronic transition from $^2H_{11/2} \rightarrow {}^4I_{15/2}$ and $^4S_{3/2} \rightarrow {}^4I_{15/2}$, respectively. Regarding the red emission band (655 nm), the multiphonon vibrational relaxations from $^2H_{11/2}$ and $^4S_{3/2}$ enrich the occupants to the electronic transition $^4F_{9/2} \rightarrow {}^4I_{15/2}$ transition. Moreover, nonradiative relaxation from the $^4I_{11/2}$ level to the $^4I_{13/2}$ results in the population of the $^4F_{9/2}$ level via energy transfer from Yb^{3+} ions. The electronic transition from $^4I_{13/2}$ to $^4I_{15/2}$ leads

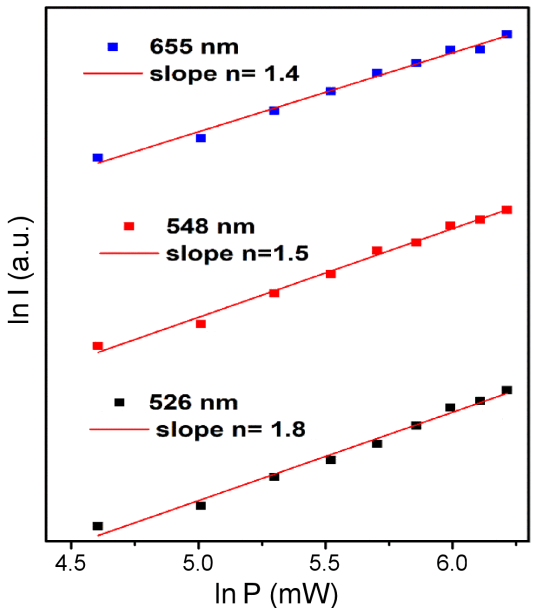

Figure 8. Bi-logarithmic plots of ln(*P*) vs ln(*I*)

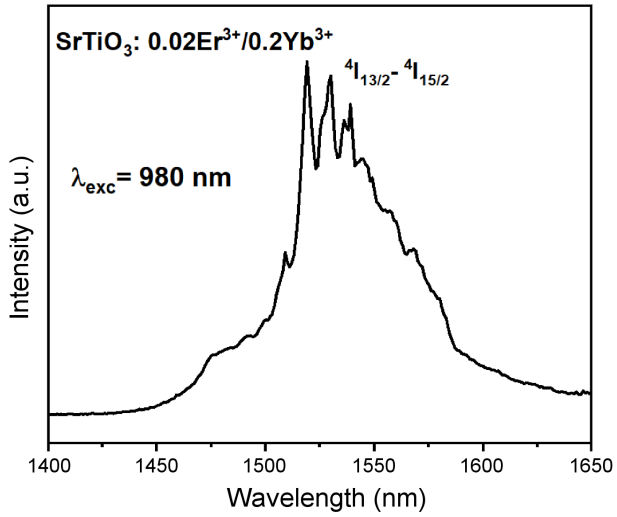

Figure 9. Down-shifting spectrum of Er^{3+}/Yb^{3+} doped $SrTiO_3$ phosphor under the 980 nm excitation

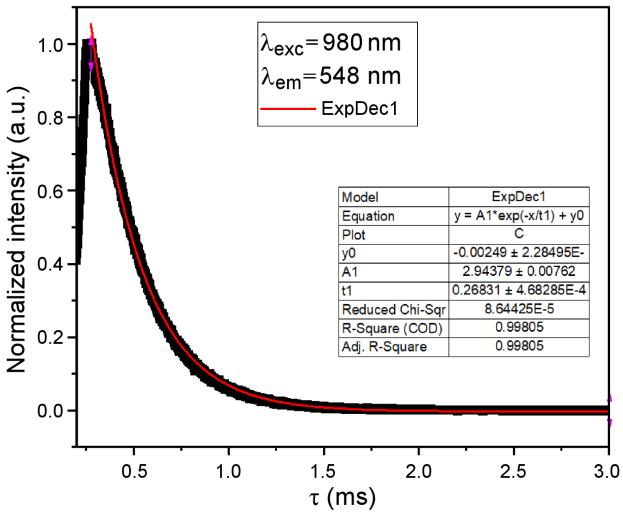

Figure 10. Decay curve of Er^{3+}/Yb^{3+} doped $SrTiO_3$ phosphor for 548 nm ($^4S_{3/2} \rightarrow {}^4I_{15/2}$) green band

to the 1535 nm NIR emission bands, which are widely used in the optical communication window for Er-doped materials [27].

The number of photons involved for the observed green ($^2H_{11/2} \rightarrow {}^4I_{15/2}$ at ~526 nm and $^4S_{3/2} \rightarrow {}^4I_{15/2}$ at ~548 nm) and red bands ($^4F_{9/2} \rightarrow {}^4I_{15/2}$, at ~655 nm) were estimated via bi-logarithmic plots for intensity vs. logarithm of laser input power (Fig. 8). The linear fit to the data fetches the slope for these bands. The slope values obtained for green and red bands were 1.78, 1.65 and 1.54, respectively. The slope value thus obtained corresponds to the non-linear optical process in which sequential absorption of two-photon involvement is confirmed for the green and red bands.

The down-shifting emission spectrum was recorded under the 980 nm NIR excitation (Fig. 9). The emission band at 1535 nm corresponds to the electronic transition $^4I_{13/2} \rightarrow {}^4I_{15/2}$ of Er^{3+} ions. There are other shoulder peaks observed, which arise due to the stark splitting of the Er^{3+} ion in the $SrTiO_3$ crystal lattice, along with the main emission peak, which corroborate the highly crystalline behaviour of the prepared ceramic material. This emission window may be used for optical telecommunications [26].

The decay kinetics of the green bands (548 nm, $^4S_{3/2} \rightarrow {}^4I_{15/2}$) and red bands (655 nm, $^4F_{9/2} \rightarrow {}^4I_{15/2}$) were also studied (Fig. 10). It is basically based on the principles of time correlated single photon counting (TCSPC). In this method, every single excited photon is counted when an excited molecule is returning to the ground state. The number of photons is time-dependent and it shows a decay with a time. The decay profile of the green band follows a mono-exponentially decay and is fitted with a single exponential decay function via $I(t) = I_0 \cdot \exp(-t/\tau)$ where $I(t)$ is the intensity after time t, I_0 is the initial intensity and τ is the lifetime of the emitting level. The mono-exponential curve fit corroborates the homogeneous distribution of activator Er^{3+} ions in the host matrix. The decay time of the green band is observed to be ~268 s, which matches with the earlier reported Er^{3+} doped samples [19,28].

The colour perception of the synthesized phosphor was studied under the different 980 nm laser input powers. The study corroborates the two-dimensional (x, y) view of the emission bands emerging from the sample. Strong green colour observed in the x, y colour coordinates (Fig. 11) complement the emission band observed at 980 nm excitation. The marginal colour tunability is observed with laser input power. The colour purity (CP) of the ceramic powder was estimated using the following equation [29,30]:

$$CP = \sqrt{\frac{(x - x_i)^2 + (y - y_i)^2}{(x_d - x_i)^2 + (y_d - y_i)^2}} \times 100 \qquad (1)$$

Table 2. Change of CIE coordinates with laser input power and corresponding colour purity

Dominant wavelength / laser input power	x	y	x_d	y_d	x_i	y_i	Colour purity
548 nm / 50 mW	0.290	0.693	0.287	0.705	0.310	0.316	96.88
548 nm / 100 mW	0.288	0.695	0.287	0.705	0.310	0.316	97.42
548 nm / 200 mW	0.283	0.699	0.287	0.705	0.310	0.316	98.53
548 nm / 300 mW	0.277	0.703	0.287	0.705	0.310	0.316	99.67
548 nm / 400 mW	0.273	0.706	0.287	0.705	0.310	0.316	100.53
548 nm / 500 mW	0.270	0.709	0.287	0.705	0.310	0.316	101.37

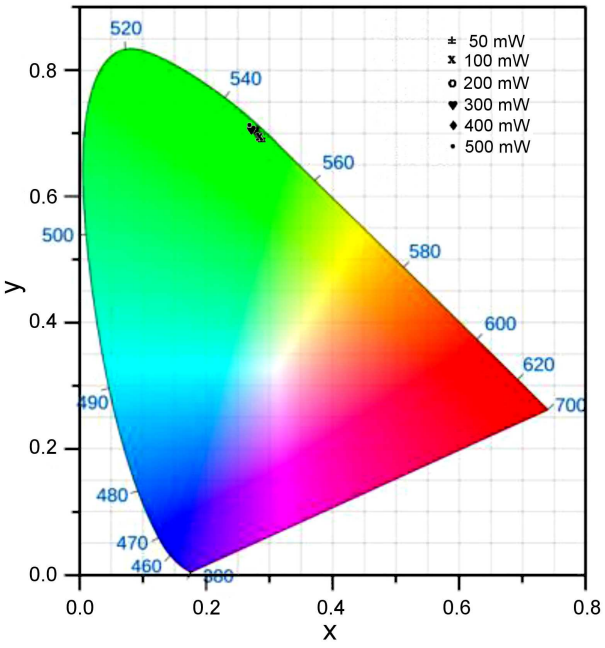

Figure 11. CIE diagram of Er^{3+}/Yb^{3+} doped $SrtiO_3$ phosphor

where (x, y) are the CIE coordinates, (x_i, y_i) are the illumination points and (x_d, y_d) correspond to the coordinates of the dominant wavelength. Changes of the CIE coordinates and colour purity with laser power were calculated using Eq. (1) and presented in Table 2. At 300 mW laser input power, ~99.67% colour purity was attained. Moreover, beyond this power, colour saturation occurs. Similar results were also obtained in Eu^{3+}/Sm^{3+} doped YPO_4 host matrices [14].

IV. Conclusions

Dual mode luminescence emitter Er^{3+}/Yb^{3+} co-doped $SrTiO_3$ phosphor was synthesized via the solid-state ceramic route at high temperature of 1200 °C. The synthesized phosphor materials exhibit outstanding green and red emission bands at 548 nm and 655 nm, which arise due to the electronic transitions $^4S_{3/2} \rightarrow {}^4I_{15/2}$ and $^4F_{9/2} \rightarrow {}^4I_{15/2}$, respectively. The power-dependent study confirms that these two bands arise due to a two-photon process. The CIE coordinates confirm the colour perception in the green region. Colour tunability was observed with varying laser input power at the 980 nm excitation. The lifetime of the $^4S_{3/2}$ is observed to be 268 µs. The down-shifting emission exhibits the band at 1535 nm, which arises due to $^4I_{13/2} \rightarrow {}^4I_{15/2}$ transition. This emission band may be crucial for laser gain and optical telecommunication applications. The current study demonstrates dual mode emission in visible and near-infrared regions for the expansion of possible applications of the up- and down-shifting phosphors for displays and optical communications.

Acknowledgement: One of the authors, Bheeshma Pratap Singh, is thankful for the financial support from DST Inspire Project (IFA-17-MS109) and DST PURSE Grant SR/PURSE/2023/169(G).

References

1. A.K. Soni, R. Joshi, B.P. Singh, N.N. Kumar, R.S. Ningthoujam, "Near-infrared- and magnetic-field-responsive $NaYF_4:Er^{3+}/Yb^{3+}@SiO_2@AuNP@Fe_3O_4$ nanocomposites for hyperthermia applications induced by fluorescence resonance energy transfer and surface plasmon absorption", *ACS Appl. Nano Mater.*, **2** (2019) 7350–7361.
2. R. Joshi, R.S. Perala, A. Ballal, S.B. Shelar, B.P. Singh, R.S. Ningthoujam, "Super bright red up-conversion in $NaErF_4$:0.5%Tm@$NaYF_4$:20%Yb nanoparticles for anti-counterfeit and bioimaging applications", *ACS Appl. Mater. Interfaces*, **15** (2021) 3481–3490.
3. L.S. Devi, M. Srivastava, R. Agrawal, R.S. Perala, R. Joshi, B.P. Singh, R.S. Ningthoujam, "Ultralow concentration in parts per trillion with nanomolar level detection for monodispersed upconversion nanoparticles of Li-co-doped $NaYF_4:Ho^{3+}/Yb^{3+}$: Potential materials in multimodal applications", *ACS Appl. Opt. Mater.*, **3** (2025) 444–454.
4. R. Agrawal, S. Patra, S.B. Shelar, C. Kumar, M. Srivastava, S. Chakraborty, R.S. Ningthoujam, "Li-doped $NaYF_4$:Ho,Yb upconversion nanoparticles for chemotherapy and radionuclide therapy of cancer", *ACS Appl. Nano Mater.*, **7** (2024) 21800–21813.
5. G. Chen, I. Roy, C. Yang, P.N. Prasad, "Nanochemistry and nanomedicine for nanoparticle-based diagnostics and therapy", *Chem. Rev.*, **116** (2016) 286–2885.
6. M. Nyk, R. Kumar, T.Y. Ohulchanskyy, E.J. Bergey, P.N. Prasad, "High contrast in vitro and in vivo photoluminescence bioimaging using near infrared to near infrared up-conversion in Tm^{3+} and Yb^{3+} doped fluoride nanophosphors", *Nano Lett.*, **8** (2008) 3834–3838.
7. Z. Xia, R.S. Liu, "Tunable blue-green color emission and energy transfer of $Ca_2Al_3O_6F:Ce^{3+},Tb^{3+}$ phosphors for near-UV white LEDs", *J. Phys. Chem. C*, **116** (2012) 15604–15609.

8. X. Huang, S. Han, W. Huang, X. Liu, "Enhancing solar cell efficiency: The search for luminescent materials as spectral converters", *Chem. Soc. Rev*., **416** [2] (2013) 173–201.
9. F. Wang, D. Banerjee, Y. Liu, X. Chen, X. Liu, "Upconversion nanoparticles in biological labeling, imaging, and therapy", *Analyst*, **135** (2010) 1839–1854.
10. B. Zhou, B. Shi, D. Jin, X. Liu, "Controlling upconversion nanocrystals for emerging applications", *Nat. Nanotech*., **10** (2015) 924–936.
11. M. Srivastava, R. Agrwal, "Codoping of yttria (Y_2O_3): Ho-Yb nanoparticles with Li increase emitted green light intensity for security ink and bioimaging", *ACS Appl. Nano Mater*., **6** [22] (2023) 20887–20898.
12. H.S. Lokesha, K.R. Nagabhushana, M.L. Chithamb, F. Singh, "Down and up conversion photoluminescence of ZrO_2:Er^{3+} phosphor irradiated with 120 MeV gold ions", *Mater. Res. Express*, **7** (2020) 064006.
13. L. Xu, Y.n Yu, X. Li, G. Somesfalean, Y. Zhang, H. Gao, Z. Zhang, "Synthesis and upconversion properties of monoclinic Gd_2O_3:Er^{3+} nanocrystals", *Opt. Mater*., **30** (2008) 1284–1288.
14. B.P. Singh, M. Srivastavab, K.V. Ramesha, M.C. Varmaa, P. Atchutha Raoc, B. Sahu, A. Bairagya, S. Devarakonda, H. Korlapati, R.S. Ningthoujam, "Nano architectonics of PEGylated YPO_4: Eu^{3+}, Sm^{3+}, Tb^{3+} doped nanoparticles: Optical and anticounterfeit application", *Ceram. Int*., **51** (2025) 6772–6782.
15. B.P. Singh, A.K. Parchur, A.A. Ansari, P. Singh, S.B. Rai, "Enhanced photoluminescence in $CaMO_4$:Eu by Gd cooping", *Dalton Trans*., **43** (2014) 4789.
16. P. Ghosh, J. Oliva, E. De la Rosa, K.K. Haldar, D. Solis, A. Patra, "Enhancement of upconversion emission of $LaPO_4$:Er@Yb core-shell nanoparticles/nanorods", *J. Phys. Chem. C*, **112** (2008) 9650–9658.
17. D. Bao, X. Yao, N. Wakiya, K. Shinozaki, N. Mizutani, "Band-gap energies of sol-gel-derived $SrTiO_3$ thin films", *App. Phys. Lett*., **79** (2001) 3767–3769.
18. F. Vetrone, J.C. Boyer, J.A. Capobianco, M. Bettinelli, "Effect of Yb^{3+} cooping on upconversion emission in nanocrystalline Y_2O_3:Er^{3+}", *J. Phys. Chem. B*, **107** (2003) 1107–1112.
19. C. Stanciu, S. Hau, G. Stanciu, C. Tihon, "Er, Yb-codoped $SrTiO_3$ ceramics: Synthesis, structural, microstructural and optical characterization", *Ceram. Int*., **51** (2025) 16771–16779.
20. O.V. Nemytova, I.V. Piir, M.S. Koroleva, D.V. Perov, A.B. Rinkevich, "Magnetic properties of nanocomposite and bulk rare earth titanates $Ho_2Ti_2O_7$ and $Yb_2Ti_2O_7$", *J. Magn. Magn Mater*., **494** (2020) 165800.
21. A.M. Dehkordi, S. Bhattacharya, T. Darroudi, X. Zeng, H.N. Alshareef, T.M. Tritt, "Synthesis of non-uniformly Pr-doped $SrTiO_3$ ceramics and their thermoelectric properties", *J. Vis. Exp*., **102** (2015) e52869.
22. R.D. Shannon, "Revised effective ionic radii and systematic studies of interatomic distances in halides and chalcogenides", *Acta Cryst*., **A32** (1976) 751.
23. A.M. Youssef, H.K. Farag, A. El-Kheshen, F.F. Hammad, "Synthesis of nano-structured strontium titanate by sol-gel and solid-state routes", *Silicon*, **10 (**2018) 1225–1230.
24. M. Harooni, A.S. Attar, "Enhanced dielectric properties and energy storage density of Mg-doped $SrTiO_3$ nanowire films", *Process. Appl. Ceram*., **16** (2022) 55–63.
25. V. Yadav, H. Cheema, R.S. Maurya, S. Kumar, P.A. Alvi1, M. Sharma, U. Kumar, "Study of structural, optical, dielectric, and electric properties of homovalently substituted Ce in $SrTiO_3$ perovskite oxide", *Ionics*, **28** (2022) 5513–5524.
26. B.P. Singh, A.K. Parchur, R.K. Singh, A.A. Ansari, P. Singh, S.B. Rai, "Structural and up-conversion properties of Er^{3+} and Yb^{3+} co-doped $Y_2Ti_2O_7$ phosphors", *Phys. Chem. Chem. Phys*., **15** (2013) 3480–3489.
27. I. Etchart, A. Huignard, M. Berard, M.N. Nordin, I. Hernandez, R.J. Curry, W.P. Gillin, A.K. Cheetham, "Oxide phosphors for efficient light upconversion: Yb^{3+} and Er^{3+} co-doped Ln_2BaZnO_5 (Ln = Y, Gd)", *J. Mater. Chem*., **20** (2010) 3989.
28. A. Patra, C.S. Friend, R. Kapoor, P.N. Prasad, "Upconversion in Er^{3+}:ZrO_2 nanocrystal", *J. Phys. Chem. B*, **106** (2002) 1909.
29. Maheshwary, B.P. Singh, R.A. Singh, "Effect of annealing on the structural, optical and emissive properties of $SrWO_4$:Ln^{3+} (Dy^{3+}, Eu^{3+} and Sm^{3+}) nanoparticles", *Spectrochim. Acta*, **152** (2016) 199–207.
30. N. Jain, B.P. Singh, R.K. Singh, J. Singh, R.A. Singh, "Enhanced photoluminescence behaviour of Eu^{3+} activated $ZnMoO_4$ nanophosphors via Tb^{3+} co-doping for light emitting diode", *J. Lumin.*, **188** (2017) 504–513.